MINISTRY OF EDUCATION AND SCIENCE OF UKRAINE
Taras Shevchenko National University of Kyiv
Faculty of Physics
Department of Nuclear Physics

Refinement of the SuperNEMO demonstrator geometry based on ^{207}Bi decay measurements

Field: 10. Natural Sciences
Specialization: 104. Physics and Astronomy
Study Program: High Energy Physics

Bachelor thesis

written by student of 4^{th} year of studies by the name of
Vladyslav Oleksandrovych Yankovskyi
Supervisor:
Mgr. Miroslav Macko, PhD.
Institute of Experimental and Applied Physics
Czech Technical University in Prague, Czechia
Departmental supervisor:
Candidate of physical and mathematical sciences
Doc. Oleg Anatoliovych Bezshyyko

Kyiv – 2023

АНОТАЦІЯ

Янковський В. О. Уточнення геометрії демонстратора SuperNEMO на основі вимірювань розпаду ^{207}Bi

Кваліфікаційна робота бакалавра за спеціальністю 104 Фізика та астрономія, освітня програма “Фізика високих енергій”. "— Київський національний університет імені Тараса Шевченка, фізичний факультет, кафедра ядерної фізики та високих енергій "— Київ "— 2023.

Науковий керівник: Miroslav Macko, PhD., Institute of Experimental and Applied Physics, Czech Technical University in Prague, Czechia

Науковий керівник від кафедри:: к.ф.-м.н., доц. Безшийко Олег Анатолійович, доцент каф. яд. фізики.

В дипломній роботі представлено надійний статистичний підхід для отримання координат 14-ти калібрувальних джерел ^{207}Bi у детекторі SuperNEMO. Джерела ^{207}Bi випромінюють електрони, лінійні треки яких реконструюються в системі відстежування частинок. Використовуючи відповідні геометричні припущення і ці треки, можна визначити положення джерел. Дослідження показало, що метод є вдалим і може досягати точності порядку кількох міліметрів або навіть краще.

Ключові слова: нейтрино, подвійний бета-розпад, безнейтринний подвійний бета-розпад, SuperNEMO, Bi-207, геометрія детектора, багатодротовий трековий детектор в режимі Гейгера.

SUMMARY

Yankovskyi V. Refinement of the SuperNEMO demonstrator geometry based on 207Bi decay measurements
Masters qualification work in specialty 104 Physics and astronomy, educational program “High energy physics”. "— Taras Shevchenko National University of Kyiv, Faculty of Physics, Department of Nuclear Physics and High Energy. "— Kyiv "— 2023.

Research supervisor: Miroslav Macko, PhD., Institute of Experimental and Applied Physics, Czech Technical University in Prague, Czechia

Research supervisor from the department: PhD of Physics and Mathematics, Assoc. Prof. Bezshyyko O., Associate Professor of Department of Nuclear Physics.

The thesis presents a robust statistical approach for extraction of coordinates of 14 ^{207}Bi calibration sources in SuperNEMO detector. ^{207}Bi sources emit electrons whose linear tracks are reconstructed in the particle tracker system. Using appropriate geometrical assumptions and these tracks the positions of the sources can be extracted. The study has shown that the method is successful and can reach precision on the order of millimiters or better.

Key words: neutrino, Double Beta-Decay, Neutrinoless Double Beta-Decay, SuperNEMO, Bi-207, detector geometry, multiwire track detector in Geiger mode.

Contents

1 Introduction

1.1 Brief history of the neutrino

At the beginning of the 20^{th} century physicists were already familiar with existence of so-called beta-decay [1]. Nevertheless, the understanding of this process was not yet complete. The decay was understood as a process when negatively charged particles (which Ernest Rutherford named "β-radiation") are emitted by the observed substance. Very soon later it was established that this mysterious β^- particle had properties of already known particle - the electron [1]. Their understanding of the process can be, therefore, expressed as:

$$(A, Z) \Longrightarrow (A, Z + 1) + \beta^- \tag{1.1}$$

Problems with such interpretation arose with the development of quantum mechanics, which postulated the discrete nature of the states of the quantum objects. The theoretical energy spectrum of β^- particles from the beta-decay should have the form of discrete delta-peaks. There are two reasons for this claim. Firstly, the energies released in the decay are determined by the difference in energy levels between the initial and final state of the nucleus. Secondly, in the decay when there is only one emitted particle, all the energy released in the decay is transformed into the kinetic energy of emitted particle. In case of α- and γ- decays, which were already known, this principle worked according to their expectation. However, in 1914, James Chadwick measured the beta spectrum and showed that it was continuous [2] (in German). It was a surprising discovery that called the law of conservation of energy into the question. Another problem was a non-conservation of the nuclear spin in the process. Since the atomic number of the nucleus has not changed in the process, the spin must also be conserved. This means that the spin of the electron that flies out of the nucleus in such a process must be an integer, which is not true.

In 1930, Wolfgang Pauli sent his famous letter to the participants of the conference in Tübingen [3] (translated into English). In the letter, he postulated the existence of a new neutral elementary particle with spin 1/2, which was emitted together with the electron during the beta-decay. He named the particle “the Neutron”. He proposed that during the decay, “the Neutron” would carry away some of the decay energy. This would mean that electron could in principle carry any

amount of the energy, not only the discrete values representing the Q-values of the decay. This could explain electron´s continuous energy spectrum. "The Neutron" non-integer spin also solves the problem of non-conservation of nuclear spin. After the discovery of (what we know today as) the Neutron by Chadwick in 1932 [4], the particle postulated by Pauli, which was estimated to be much lighter, was renamed "the Neutrino" (Italian diminutive for Neutron). The discovery of the neutron allowed Fermi to build the theory of beta-decay, which explained how exactly such a neutral particle as a neutrino could be produced by nucleus. According to our current understanding of the theory of β^--decay, a neutron (n) in the nucleus transforms into a proton (p) by emission of an electron (e) and an antineutrino ($\bar{\nu}$) (neutrino's antiparticle):

$$n^0 \Longrightarrow p^+ + e^- + \bar{\nu} \tag{1.2}$$

Neutrinos were finally detected in an experiment in 1956 by Clyde Cowan and Frederick Reines [5]. For this discovery, only Frederick Reines was awarded the Nobel Prize in 1995, because Clyde Cowan died in 1974.

The Standard Model (the SM) is currently the most successful model in particle physics. It combines all elementary particles of matter known at the moment, and particles carriers of three of the four known interactions: Strong, Weak and Electromagnetic (Gravitational interaction is currently not quantized). Carriers of these forces are gauge bosons, particles with integer spin while particles of matter in the SM are fermions (half-integer spin particles). Based on the SM neutrinos can be described in the following way: a neutral fermion, with half-integer spin (1/2) and interacting only via the Weak interaction. It exists in the form of one of three flavors and is massless. But the last statement turned out to be invalid, after the discovery of process called "neutrino oscillations".

As a result of a proton-proton chain reaction in the core of the Sun, electron antineutrinos are produced [6]. In the 1960s, Raymond Davis, Jr. and John N. Bahcall tried to detect these neutrinos. They constructed an experiment known as the Homestake experiment [7]. The measured detection rate was calculated to be 2.56±0.32 SNU[1] [8]. This was unexpected because according to the Standard Solar Model they expected a value of 9.3±1.3 SNU [8]. This meant an inexplicable discrepancy between the theory and the experiment. Both the theoretical model

[1]SNU – Solar neutrino unit denotes one neutrino capture per 10^{36} nuclei every second

and the experiment had to be revised. Nevertheless, after the effort of the whole experimental and theoretical neutrino scientific society both aspects seemed to be correct. The problem was finally explained by existence of so-called neutrino oscillations. According to this concept the (anti)neutrinos can change their flavour during their flight. The purely electron antineutrinos produced in the Sun undergo oscillations into the other flavours (muon and tau) and neutrinos of all three flavors reach the Earth. Unfortunately, all the experiments were designed to be sensitive only to the electron neutrinos, which gave rise to the Solar Neutrino Problem. An improved Super-Kamiokande experiment in 1998 proved the existence of neutrino oscillation by observation of the oscillation of atmospheric muon neutrinos into the tau flavour [9]. One year later, in 1999, the Sudbury Neutrino Observatory managed to measure the rate of solar neutrinos for all flavors at the same time, and the results in 2001, confirmed the existence of the neutrino oscillation and solved the Solar neutrino problem [10]. For the discovery of neutrino oscillations Arthur B. McDonald (SNO) and Takaaki Kajita (Super-Kamiokande) received the Nobel Prize in 2015.

Now let us understand why the neutrino oscillations can only exist if neutrinos have at least two states with non-zero masses. If we consider two bases for known neutrinos: flavour states $(\nu_e, \nu_\mu, \nu_\tau)$ and mass states (ν_1, ν_2, ν_3), then one can be expressed by a linear combination of the other using a unitary transformation matrix $U_{\alpha i}$:

$$|\nu_\alpha\rangle = \sum_i U_{\alpha i} |\nu_i\rangle \,, \tag{1.3}$$

where ν_α symbolizes a flavor state and ν_i symbolizes a mass state. $U_{\alpha i}$ is a unitary mixing matrix, so-called PMNS (Pontecorvo – Maki – Nakagawa – Sakata) matrix. Without loss of generality, if we consider a simplified case of oscillation of only two neutrino states α and β we can express the probability of oscillation as (for derivation see [11]):

$$P(\nu_\alpha \to \nu_\beta) = \sin^2(2\theta) \sin^2\left(\frac{\Delta m_{ij}^2 L}{4E}\right) \tag{1.4}$$

Here, L is the is the length of the neutrino's path, E is energy of the neutrino and $\Delta m_{ij}^2 = m_i^2 - m_j^2$ is the squared difference between the masses of the mass states i and j. Since the detection of ν_μ and ν_τ reaching the Earth from the Sun

has already been confirmed, the probability $P(\nu_\alpha \to \nu_\beta)$ of changing the flavour is non-zero. Hence, θ (so-called "neutrino mixing angle") and Δm^2_{ij} cannot be zero. Therefore, there should be at least one non-zero mass state of the neutrino (at least two non-zero mass states in the realistic case of the three neutrino families).

1.2 Double Beta-Decay

In 1935, Maria Goeppert-Mayer proposed the theory of the existence of a process in which two neutrons bound in a nucleus turn into two protons at the same time, with the emission of two electrons and two electron antineutrinos [12]:

$$(A, Z) \Longrightarrow (A, Z+2) + 2e^- + 2\bar{\nu}_e \tag{1.5}$$

The decay was already observed for several isotopes (^{82}Se, ^{76}Ge, ^{100}Mo etc.). It is extremely rare, with a half-lives for different isotopes ranging from 10^{18} yr to 10^{24} yr (see table 1.1). In 1939, Wendell H. Furry proposed another process called *Neutrinoless Double Beta Decay* ($0\nu\beta\beta$) [13]:

$$(A, Z) \Longrightarrow (A, Z+2) + 2e^- \tag{1.6}$$

It is based on the assumption that the neutrino is its own antiparticle (Majorana particle). The half-life ($T^{0\nu}_{1/2}$) of this process is related to the (effective) mass of neutrinos by the following formula:

$$\frac{1}{T^{0\nu}_{1/2}} \sim |m_{\beta\beta}|^2 G^{0\nu}(K, Z)|M^{0\nu}|^2, \qquad m_{\beta\beta} = \sum_i U_{ei} m_i, \tag{1.7}$$

where K is the kinetic energy emitted in the process, $G^{0\nu}(K, Z)$ is phase space factor (computable by theory), $M^{0\nu}$ is nuclear matrix element of $0\nu\beta\beta$ which can be obtained by the means of the nuclear structure theory and it is difficult to compute. In this expression, the effective neutrino mass $m_{\beta\beta}$ is a linear combination of the basis of the neutrino mass with the coefficients of the PMNS matrix.

The observation of $0\nu\beta\beta$ would confirm that the neutrino is of Majorana nature. In fact, today it is the only process which could help us to prove the Majorana nature of neutrinos. Furthermore, observation would provide a value of its half-life which could help us to calculate the effective neutrino mass based on the equation 1.7. The search for this process is very important for neutrino physics. It was not

observed yet so only the lower limits of half-lives were reported. The highest lower limits are currently of the order of 10^{25}-10^{26} yr (table 1.1) in dependence of the observed nucleus and the experiment.

Isotope	$T^{2\beta}_{1/2}[yr]$	$T^{0\beta}_{1/2}$[yr]	Experiment
^{76}Ge	$(1.926 \pm 0.094)\times10^{21}$	$>1.8\times10^{26}$	GERDA[14]
^{82}Se	$(8.6 \pm 0.16)\times10^{19}$	$>3.6\times10^{23}$	NEMO-3, CUPID-0[15, 16]
^{100}Mo	$(6.81 \pm 0.39)\times10^{18}$	$>1.1\times10^{24}$	NEMO-3[17, 18]
^{116}Cd	$(2.74 \pm 0.18)\times10^{19}$	$>1.0\times10^{23}$	NEMO-3[19]
^{130}Te	$(7.71 \pm 0.16)\times10^{20}$	$>2.2\times10^{25}$	CUORE[20]
^{136}Xe	$(2.21 \pm 0.27)\times10^{21}$	$>1.07\times10^{26}$	KamLAND-Zen[21, 22]
^{150}Nd	$(9.34 \pm 0.66)\times10^{18}$	$>2.0\times10^{22}$	NEMO-3[19]

Table 1.1: Recommended half-life values of $2\nu\beta\beta$ to ground state of daughter nucleus (second column), and lower limits at 90% C.L. set for the half-lives of $0\nu\beta\beta$ for chosen isotopes

1.3 Double Beta-Decay experiments

Program of Double Beta-Decay (DBD) research is already several decades old. Regardless of the type of the process, the detectors can measure only the two electrons because neutrinos escape undetected in the case of $2\nu\beta\beta$. Despite this, $0\nu\beta\beta$ can be distinguished from $2\nu\beta\beta$ by the comparison of the spectra of the sum of the electron energies (see figure 3.5). In case of $0\nu\beta\beta$ both electrons carry all of the decay energy and the sum of their energies is always the same - the Q value of the decay. In the case of $2\nu\beta\beta$ the antineutrinos take away some of the energy and the sum of the electron energies forms a continuous spectrum.

The experiments searching for $0\nu\beta\beta$ can be divided into two basic categories: homogeneous and heterogeneous detectors. Homogeneous detectors take advantage of decay isotopes which can be also used as a detector material. In this type of experiments the source is, therefore, a detector at the same time. Heterogeneous detectors use the source and the detector as two separated systems. The following (non-exhaustive) list summarizes examples of experiments according to their technological approach:

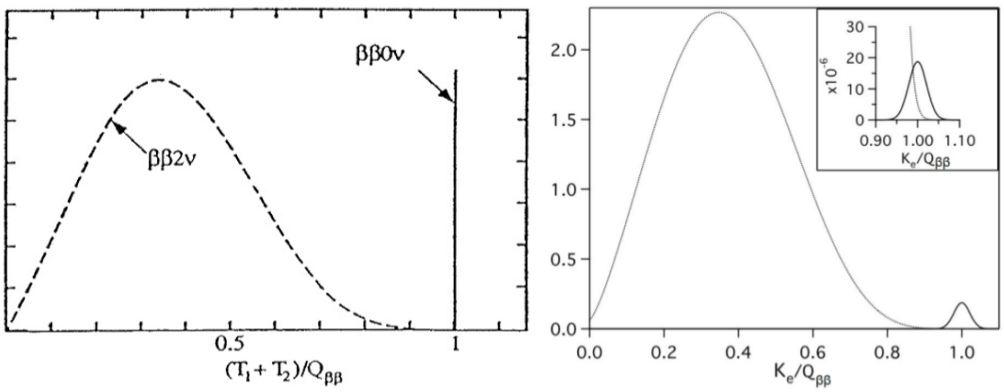

(a) (b)

Figure 1.1: DBD spectra. The horizontal axis represents the sum of the kinetic energies of individual electrons ($K_e = T_1 + T_2$), in units of Q-value of the decay denoted by $Q_{\beta\beta}$. (a) Theoretical spectrum. (b) Experimental spectrum assuming only the effect of detector resolution.

Semiconductor experiments (homogeneous detectors): The signals here are received using semiconductors. Most often, it is the Germanium semiconductor diodes, which provide high registration efficiency and excellent energy resolution. Examples: LEGEND[23], GERDA[24], MAJORANA[25] (Ge diodes).

Bolometer experiments (homogeneous detectors): Bolometers are low-temperature calorimeters capable of measuring the energy of an incoming particle using the fact that it is able to increase the temperature of the bolometer material (such as $^{116}CdWO_4$, $^{40}Ca^{100}MoO_4$ or $Zn^{82}Se$) in proportion to its energy. Examples: AMoRE[26], CUPID[27], CUORE[28].

TPC and Scintillator experiments (homogeneous detectors): Time Projection Chambers use ionization electrons and anodes that attract them, which makes it possible to reconstruct the track in three dimensions. The material with which the ionizing particle interacts can be a scintillator, which makes it possible to profit from ionization and scintillation light in coincidence. Such scintillators are usually liquid (or Gas) ^{136}Xe and crystal ^{48}Ca. Examples: KamLAND-Zen[29], CANDLES[30], EXO[31, 32].

Tracko-Calorimeter experiments (heterogeneous detectors): This type is based on a combination of a tracking system and calorimeters that provide information on the energy and momentum with the location of the particle, respectively. The main advantage of this approach is excellent suppression of the background, according to the typology of the event. Examples: NEMO-3[33], SuperNEMO[34],

NEXT[35].

2 The SuperNEMO experiment

As indicated in the previous paragraph, the SuperNEMO detector takes advantage of the technology combining the calorimeter technology with particle tracking. The main advantage of this approach is the possibility to obtain full topology of the events and perform the particle identification. This allows for improved background rejection and to study the distribution of angles between the two emitted electrons (so-called angular distribution). SuperNEMO detector consists of four main systems: *decay source* ^{82}*Se source foils*, *tracking detector*, *calorimeter* and ^{207}*Bi energy calibration system* (see figure 2.1a).

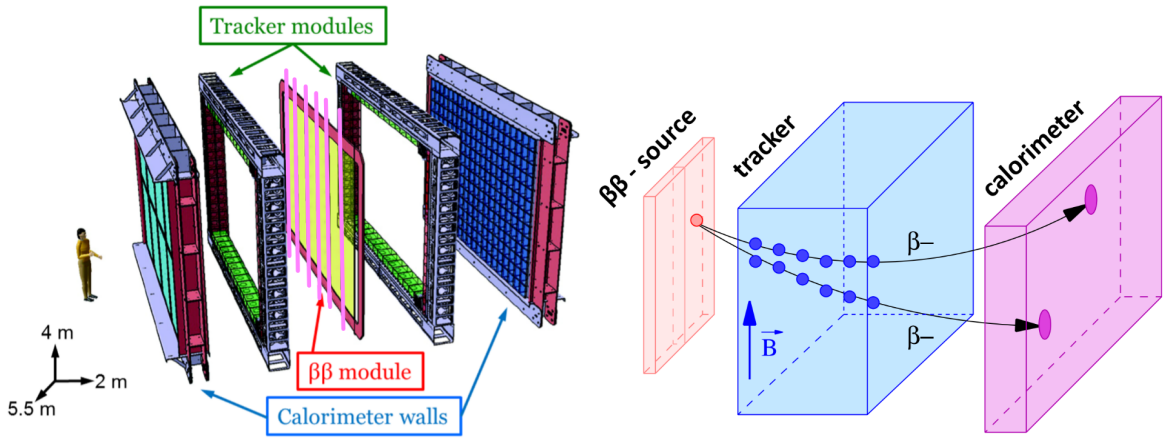

(a) (b)

Figure 2.1: (a) Schematic of the SuperNEMO detector design. The pink lines in the figure represent 6 gaps between ^{82}Se foils. Stepper-motor based system can automatically insert and remove 42 ^{207}Bi calibration sources (7 sources per column) into these gaps. (b) The schematic representation of the tracko-calorimetric approach (one half of detector). The decay happens in the source foil, subsequently, the individual electrons tracks are reconstructed by tracking detector and the individual electron energies are measured separately in the segmented calorimeter.

The electrons emitted from the $\beta\beta$ source pass through the tracking detector, which allows us to obtain information about the track of the particle, and when it reaches the segmented calorimeters, we obtain information about the energy of this individual particle (see figure 2.1b).

2.1 Source Foils

There are several important requirements for a decay source to be used for DBD research. The first is a purity of the source. There are isotopes such as ^{208}Tl or ^{214}Bi which are present in the Earth's crust and they can contaminate the decay source in the production process. These isotopes can mimic the $0\nu\beta\beta$ signal in the detector and, therefore, should be carefully monitored and eliminated if possible. ^{208}Tl is particularly dangerous because it emits gammas of 2.615 MeV. By fast succession of two Compton scatterings inside of the decay source, such gamma is capable to produce two electrons. Sum of kinetic energies of such electrons is never higher than 2.615 MeV. Higher the energy of the double beta decay $Q_{\beta\beta}$, the less it is affected by the internal background from the ^{208}Tl. The second important factor for choice of decay isotope is the natural abundance of the isotope and how difficult is the technology of its enrichment. The greater the enrichment, the greater the chances of observation $0\nu\beta\beta$.

^{82}Se was chosen for the SuperNEMO experiment due to the high value of $Q_{\beta\beta}$ = 2996 keV and its favourable natural abundance 9.2% [36]. ^{82}Se is placed in the detector as 34 thin foils with a total mass of 6.23 kg of Selenium which accounts for 6.11 kg of ^{82}Se. Enriched selenium in powder form is applied to Mylar foil for mechanical strength [37]. The source foils are relatively thin with only around 40 mg/cm^2.

2.2 Particle tracking system

SuperNEMO uses a wire-chamber tracking as a tracking detector[38]. It is a system of drift cells operating in the Geiger mode (voltage around 1600 V), therefore, they are also called Geiger cells. Each of them is composed of an anode steel wire with 40 µm diameter surrounded by 12 grounded field-forming wires with 50 µm diameter (shared between neighbouring cells), and cathodes at both ends of the cell. In total, there are 9 rows of 113 such cells on each side of the source, therefore, total number is 2034. Inside the tracker, gas is used, which is a mixture of 95% helium, 4% ethanol and 1% argon.

A charged particle passes through the cell and excites gas atoms from which electrons escape, which as a result move towards the anode (figure 2.2). In the region of a strong field, ionization will begin to create ultraviolet light, which will

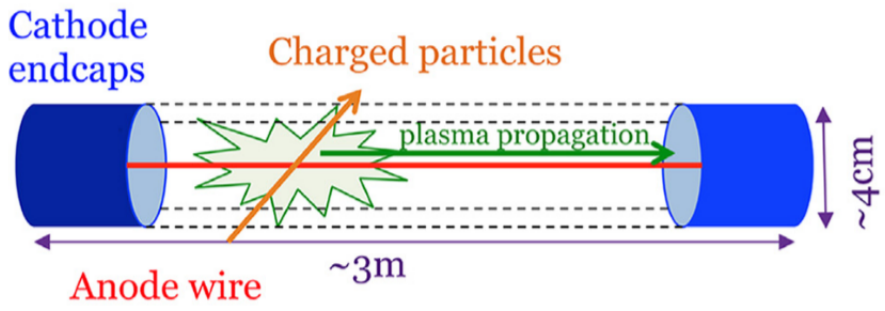

Figure 2.2: Detection principle of one SuperNEMO Geiger cell. The scheme shows a charged particle (e.g. electron) passing through a Geiger Cell. The process is explained in more detail in the text. The red long line represents anode. Geiger cell is "standing" in the SuperNEMO detector so its length is along the vertical direction.

cause new ionization, forming a chain reaction. As a result, ions from this region will propagate along the anode to the corresponding cathodes until they recombine. The time difference between the signals at the top and bottom cathode give information about longitudinal location of the track. The drift time of the initial electron avalanche to the anode (perpendicular to the anode) gives information about the shortest distance of the particle track to the anode. The signal from ensemble of such Geiger cells allow a 3D track reconstruction.

2.3 Calorimeters

A segmented calorimetric system of SuperNEMO detector is used to determine the kinetic energy of the electrons from the decay [39]. It consists of three parts surrounding the detector from all four vertical sides as well as from top and bottom. Two walls in the yz plane are the biggest and, therefore, they are referred to as main calorimeter walls. On the sides perpendicular to ^{82}Se foils there are two narrow walls called "X-calo" walls. Finally, on top and the bottom one finds segments called "g-veto" (figure 2.3a).

The whole calorimeter is composed of smaller units called Optical Modules (OMs) 2.3b. Each module consists of a plastic scintillator coupled with photomultiplier tube (PMT) (figure 2.3c). The scintillator is a block of polystyrene with addition of wavelength shifters pTP (0.6%) and POPOP (0.05%)[40]. For different walls of the calorimeter, the optical modules differed slightly. Thus, gveto consists of 64 modules with an energy resolution of 15% at 1 MeV, Xcalo - of 128 modules

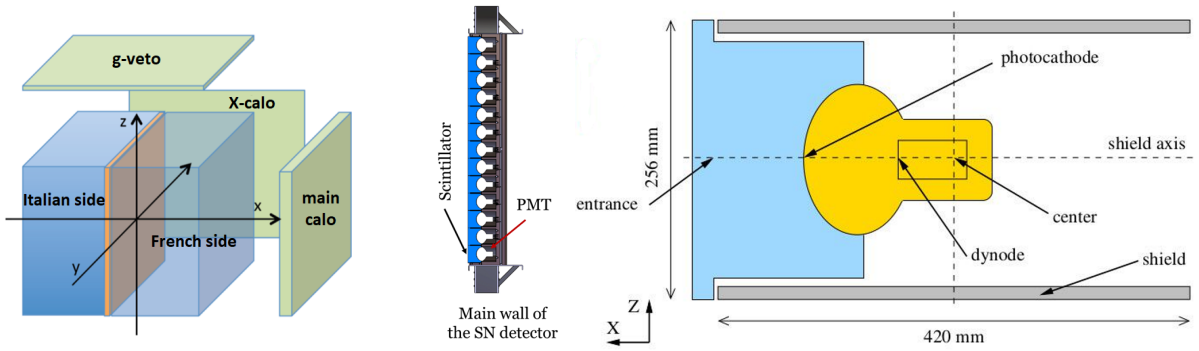

(a) (b) (c)

Figure 2.3: (a) Naming of the calorimeter segments and their position in the context of standard SuperNEMO coordinate system. Each of the calorimeter segments depicted in the figure have their own counterpart on the other side of the detector. Orange plane represents ^{82}Se source foils. Blue volumes represent two halves of the tracker. (b) Vertical cross-section of the main calorimeter wall composed of individual Optical Modules. (c) Detailed description of Optical Module.

of 12% at 1 MeV, and the main calorimeter - of 520 modules with 8% at 1 MeV, and that in total is 712 modules for the entire calorimeter system.

2.4 ^{207}Bi calibration system

SuperNEMO is using a set of ^{207}Bi sources for energy calibration. ^{207}Bi decays via electron capture which leaves the daughter nucleus ^{207}Pb in excited state. In the most of the cases ^{207}Pb deexcites by emission of gammas of 570 keV or 1064 keV. Occasionally, deexcitation gamma is absorbed by electron from the K, L or M atomic shells of ^{207}Pb (internal conversion). In these cases, instead of 570 keV and 1064 keV gammas, mainly (but not only) 482 keV, and 976 keV K-shell electrons are emitted. These electrons play the most important for the energy calibration of the SuperNEMO detector.

Calibration sources need to be removed from the sensitive zone of the detector after the calibration. However, the detector is sealed to preserve its internal atmosphere, so it is impossible to manually remove these sources. Therefore, the calibration system in SuperNEMO uses an automatic deployment system developed by group from University of Texas at Austin [41].

In $\beta\beta$ module (figure 2.1a) between the strips of ^{82}Se foil there are six thin gaps intended for the calibration system. This system consists of 6 plumb bobs, each

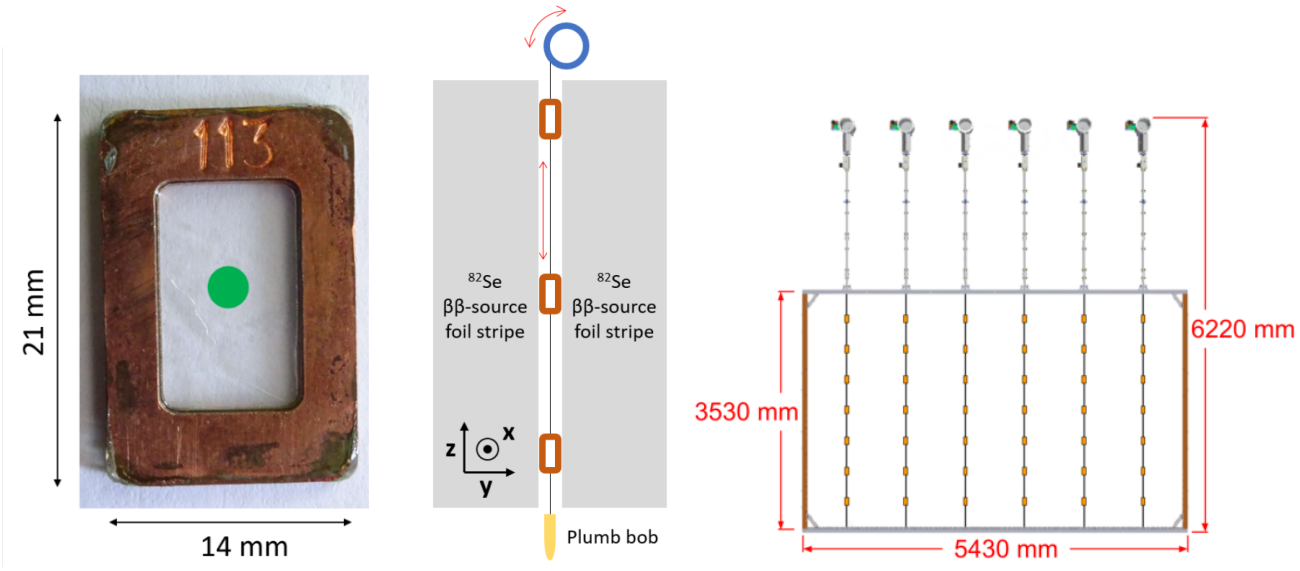

(a) (b) (c)

Figure 2.4: (a) Photo of the SuperNEMO calibration sources. The green circle indicates the location of the ^{207}Bi droplet which is normally not visible by naked eye. (b) Simplified scheme of the ^{207}Bi deployment system.

connected by steel wires to a corresponding wheel at the top of the SuperNEMO module (figure 2.4c). Wheels can be rotated by a stepper motor with high precision. Between the plumb bobs and the wheel in the deployed state, 7 calibration sources are attached to two steel wires. With the help of a stepper motor, these sources can be placed or removed in the SuperNEMO detector (figure 2.4b).

SuperNEMO uses 42 ^{207}Bi sources of activity around 120 - 145 Bq. Each source has a form of a droplet of ^{207}Bi placed between two transparent mylar foils and sealed by a rectangular copper frame (figure 2.4a). The radius of the droplet is about 1.5 mm [42]. Therefore, for practical purposes, the individual ^{207}Bi sources can be considered as point-like sources.

2.5 Current status of the detector

The SuperNEMO detector is placed in the Europe´s deepest underground laboratory LSM (Laboratoire Souterrain de Modane) in Modane, France. Before 2021, all the source foils, calorimeter parts and the tracker were already delivered and installed underground. In 2021, the sealing of the detector was performed in order to achieve gas tightness. At the end of 2021, sealing was completed and a gas overpressure of 10 mbar was achieved. At the beginning of 2022, the calorimeters

were running and taking commissioning data. In mid 2022 - first data acquisition (DAQ) board for tracker (out of three) was delivered. From this point it was possible to take data with one third of the tracker. Thanks to this, data run number 728 used in this work was measured in June 2022. In 2023 remaining DAQ boards were installed and first data with all calorimeters and tracker were measured. In 2024, shielding is expected to be installed. With the shielding it will be possible to start measurements of the physics data.

3 Study of the positions of ^{207}Bi sources

SuperNEMO is currently in the final stage of commissioning. The first physics runs are expected in 2024, and now the detector is being tested and tuned. The particle tracking system in the SuperNEMO experiment is a relatively precise tool to study detector geometry. For example, it can help to determine the positions of the ^{207}Bi calibration sources inside of the detector. By application of appropriate statistical methods, one can determine these positions from the decay data and compare them with the "ideal" values from the blueprints. This approach, if successful, can serve to fine-tune the geometrical model of the detector in the simulation. The ability to recognize the difference between the values from the design and the detector blueprints is limited by the accuracy of the tracker. Therefore, such study can also be understood as a study of the limits of particle tracking accuracy. In any case, useful information about the detector will be obtained.

3.1 Definition of the problem

In order to ensure quality of the energy calibration, it is crucial to determine whether the electron originated in the calibration source or whether it is a result of some other unwanted process in the detector. The blueprints of the detector offer the estimation of the positions, nevertheless, the reality might be slightly different. It is, therefore, necessary to study the positions "as seen" by the tracker. Such knowledge will lead to design of more efficient data cuts for energy calibration. The electrons loose relatively small amount of the energy in the tracking gas depending on the distance they cover inside of the tracker. With appropriate mathematical model these losses can be estimated and partially corrected for by precise knowledge of the distance. The distance can be properly calculated only

if the source positions are known with sufficient precision. The goal of this thesis is to find suitable statistical methods to extract the positions of the ^{207}Bi sources relative to two halves of the tracking system. The study is based on the detection of the electrons emitted from these sources.

In the thesis, the terminology generally accepted within the collaboration is used to describe some parts of the detector. The detector is located in the underground laboratory in Modane (LSM), which is close to the border between France and Italy. If one uses the coordinate system introduced in the figure 2.3a, then the half of the tracker placed on the side with positive values of x is called the "French tracker" because it points to France. Analogically, the half of the tracker placed on the side with negative values of x is called the "Italian tracker". The collaboration also uses a naming convention for the detector sides along the y-axis. The part facing the mountain is called the "mountain side" ($y < 0$), the part facing the tunnel outside is called the "tunnel side"($y > 0$).

The tracking detector is composed of four separate sections (C0-C3)[43], two on the French side and two on the Italian side. In 2020, half of the tracker on the Italian side had to be lifted up (in z-direction) by lower units of millimeters due to technical difficulties with the supporting structure. Hypothetically, this could have caused negligible misalignment's. Among the other goals, the aim of this work is to study these hypothetical misalignment if it would be within the reach of the tracking precision. This is why we assume, for the purpose of the work, two independent coordinate systems for French and Italian side trackers. If these two coordinate systems would share common origin within the precision of the particle tracking, no misalignment could be reported.

3.2 Brief description of the tracking algorithm and the source data

The whole analysis presented in the thesis is based on the data from commissioning run no. 728. The data were measured on 21^{st} of June 2022 with the ^{207}Bi sources deployed. The data were measured during 2.5 hours and shielding of the detector was not yet installed. At that time, only one of three data acquisition boards for tracker were available and installed. Therefore, only one third of the tracker cells (on the "mountain" side, i.e. $y<0$) were active, see figure 3.1. This is

why only two columns of ^{207}Bi (14 sources) were deployed. The calorimeter, which is important as an event trigger condition was fully operational. ROOT software [44] was used for all the data analysis in the thesis. The input data for the study which were obtained by track reconstruction were also in the format of ROOT file.

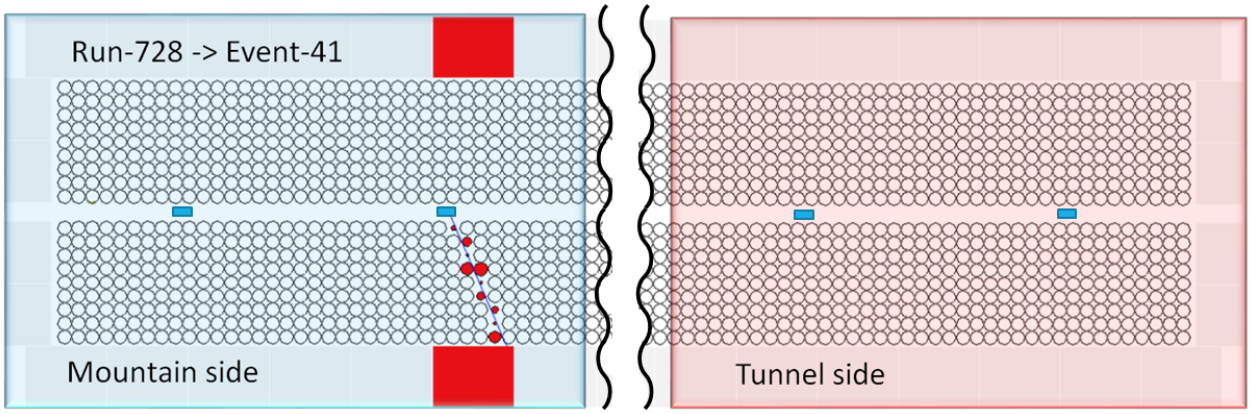

Figure 3.1: Top view of the detector used for representation of the separate events. The grid of circles represents a tracker, where each individual circle is a Geiger cell 2.2, and the grey rectangles surrounding them are OMs 2.3c. Source foils are located in the gap between the two parts of the detector. The blue rectangles inside these gaps indicate the columns of the ^{207}Bi calibration sources. For each event, the parameters of the triggered Geiger cells (red circles) and OMs (red rectangles) are known. The middle sector of the detector is not shown in the picture.

Using the system of these triggered cells, the electron tracks are reconstructed by the method based on Legendre transform [45] (blue lines). The radii r of the red circles represent measured distances (in xy plane) between the linear trajectory of the electron and the anode wire of a given hit. Z coordinate of this circle is measured along the cell using plasma propagation delay to both cathodes at the top and bottom of the cell (for details see figure 2.2). Resulting fit is a straight line in three dimensions defined by four parameters a, b, c and d:

$$y = ax + b, \qquad z = cx + d. \tag{3.1}$$

As discussed previously, two halves of the tracker (French and Italian) are considered as two separate detector systems. Therefore, the tracks are fitted separately on Italian side and separately on the French side. The ^{207}Bi sources are placed in the middle plane of the detector, therefore the electrons emitted from the sources should always be emitted either to one side or another one. In the figure 3.2 it is

possible to observe cross section vertices of the tracks fitted by French side tracker with plane x = 0 mm.

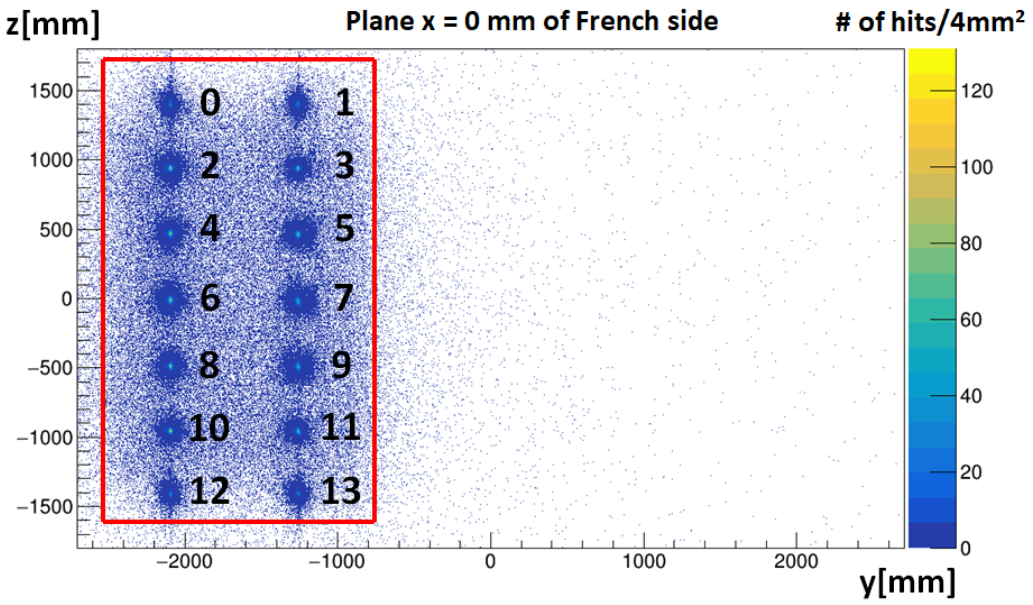

Figure 3.2: Intersection vertices between the track fits from run no 728 and plane x = 0. Only the tracks emitted to the French side were used to produce this plot. The numbers next to each hot spot is used to identify individual sources throughout the whole thesis. The red rectangle represents the so-called hotspot area, which will be used in the future.

The figure shows hot spots, which represent apparent sizes of 14 calibration sources (7 in each column) in plane x = 0 mm. In order to study the source x, y and z positions of these sources in more detail it is necessary to define a statistical method to extract these values.

3.3 "The spaghetti hypothesis"

As mentioned in section 2.4 ^{207}Bi sources are point-like electron sources with very well defined equidistant positions. This makes them a great reference points for the experimental measurements of detector dimensions. According to the figure 2.3a the ^{207}Bi sources should be placed in the plane defined by x = 0. In the study we decided to test this assumption, therefore, we did not consider the x-coordinate of the sources fixed - see figure 3.3.

Consider the calibration source ^{207}Bi as a point-like object emitting electrons. Electrons will leave the source in two directions, to the French side and to the

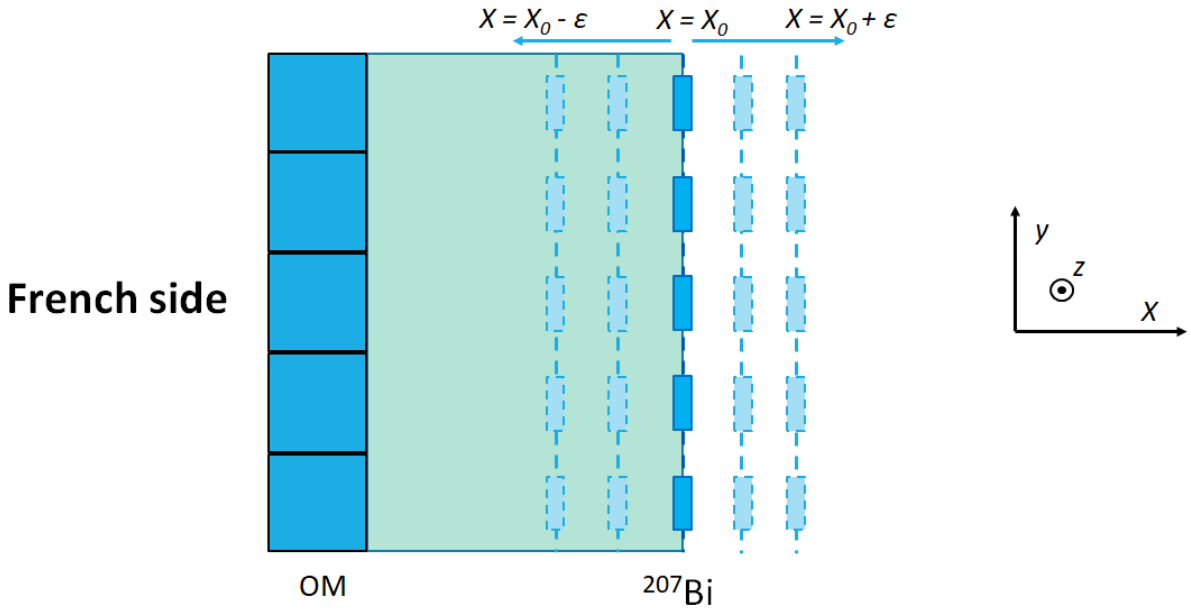

Figure 3.3: Depiction of possible positions of the ^{207}Bi sources in the x-direction. In each scenario it is assumed that the sources are at the same x-coordinate.

Italian side. According to our methodology, we consider the two sides of the detector as two "separate experiments", therefore, when studying one of them, we will use only electrons moving in the corresponding direction, and extrapolate their tracks to both infinities. We define set of 2N+1 equidistant parallel planes defined by x = X_0 - Nε, X_0 - (N-1)ε, ..., X_0 - ε, X_0, X_0 + ε, ..., X_0 + (N-1)ε, X_0 + Nε. Here, ε defines a distance (step) between two neighbouring planes and N is a number of planes on one side. X_0 represents x-coordinate of the ^{207}Bi sources as seen in the data. We aim to extract this value. Each of the planes share a vertex with each of the lines (extrapolated to infinities on the both sides) obtained by the track reconstruction from French tracker. The situation is depicted in the figure 3.4a. The same process can be repeated also for the tracks reconstructed based on the hits from the Italian side tracker. One would obtain similar picture but this time in the coordinate system of Italian side tracker.

It should be noted that in an "ideal case", all electron tracks would have a vertex exactly at the source, and then on the plane x = X_0 one could see a single point of intersection. However, in reality, the reconstructed tracks being a subject of measurement are not perfectly precise. As a result, with a large number of tracks, one should expect to observe a system of circles (or ellipses) in all the planes. For the purpose of this work we will call these elliptic cross sections as Cross-Sectional Ellipses or CSEs for a given plane defined by x coordinate. Note

that, under this definition we understand a circle as a special example of and ellipse. The most important assumption on which the whole study is build we named "the spaghetti hypothesis" and states following: **"the x-coordinate of the ^{207}Bi source position is located in the plane with the smallest CSE"**.

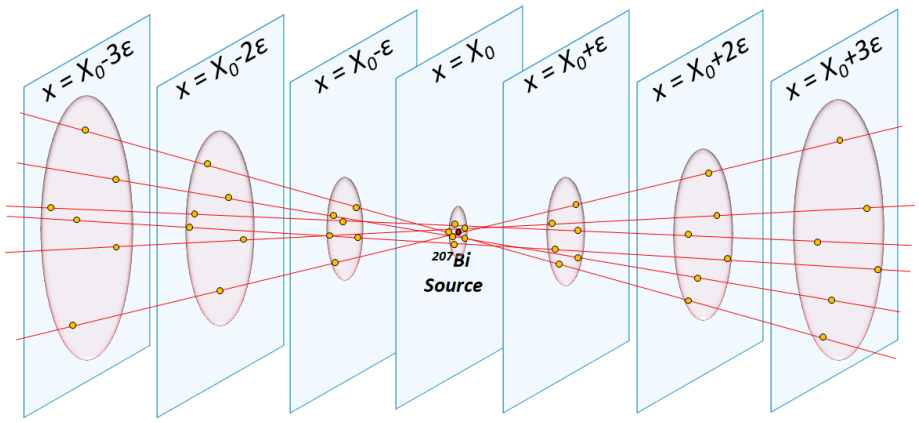

(a)

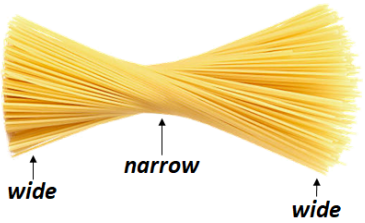

(b)

Figure 3.4: (a) Electron tracks emitted from a single ^{207}Bi source to one (e.g. "French") side are forming a shape similar to the cone. If one extends these straight tracks to both infinities, one obtains set of tracks resembling two cones merged by the tips. This shape is similar to the pack of spaghetti twisted in the middle. This process can be also repeated separately with the electron tracks emitted to the other (i.e. "Italian") side of the detector. (b) The pack of spaghetti, twisted in the middle. It can be seen that the narrowest part of the pack is in the middle

3.4 Calculation of y and z positions of the CSEs

When we talk about CSE for a given plane defined by its x-coordinate it is important to find its position and border and to find a suitable algorithm capable to extract it automatically. At the beginning, I tried to use a simple two-dimensional fit of the distributions in yz plane. This attempt was unsuccessful. Such a distribution should be fitted by some unknown distribution f(y,z) which would be

elliptically symmetric. It would need at least two parameters y_0 and z_0 for the center, another two parameters for semi-axes of the ellipse a and b and at least another one as a normalization constant. Moreover, one would need to assume some radial dependence of the function which turned out to be difficult to come up with. Therefore, such attempt to perform a fit with five parameters with vaguely defined radial dependence turned out to be impractical.

One possible solution to this problem I found in the article by R. N. Rattihalli et al. [46]. The article offers a convenient and simple non-parametric test of spherical symmetry around an arbitrary point (y_0, z_0) in yz plane without need to assume radial dependence of two-dimensional distribution.

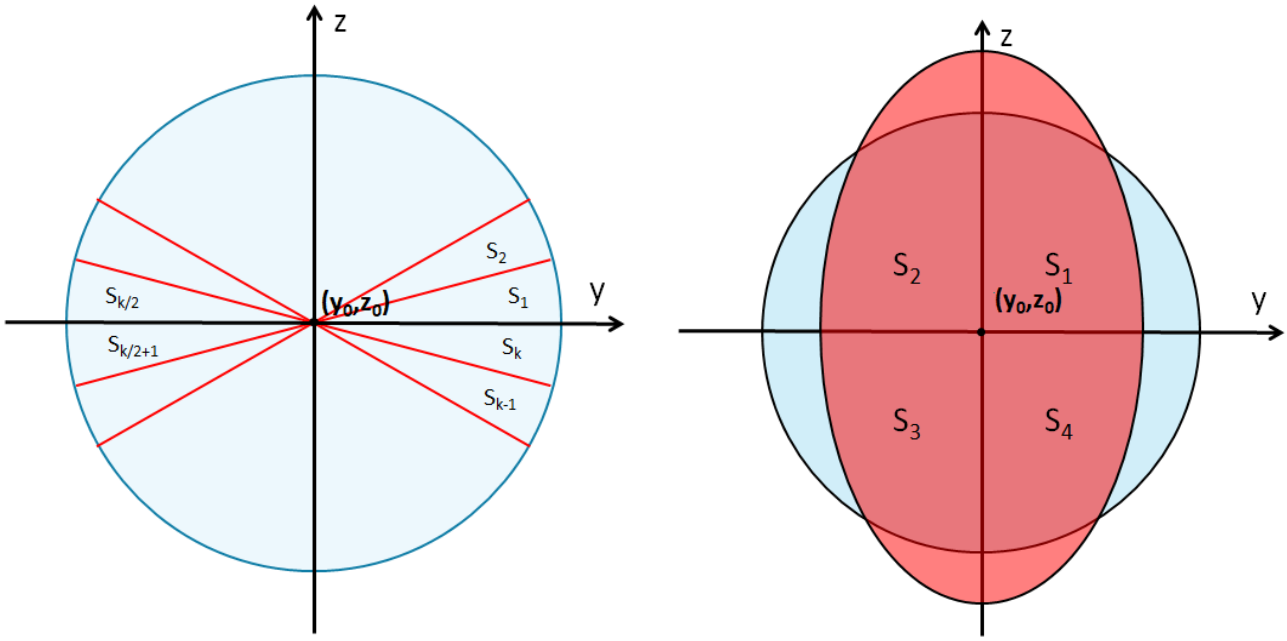

(a) (b)

Figure 3.5: (a) The circle is divided into k sectors around point (x_0, y_0) (b) Symmetry for circle and ellipse

Method works in a following way. Consider a circle of radius R, divided into k equal radial sectors around a point of expected symmetry (figure 3.5a). If the two-dimensional distribution of the vertices express the radial symmetry (around chosen point), then the probability that a random vertex would appear in any of the sector S_j is $p_j = 1/k$. It is possible to statistically estimate the spherical symmetry of the distribution sample of random events around the point (y_0, z_0) using the Chi-square approach introduced in [46]:

$$\chi^2 = \frac{k}{n} \sum_{j=1}^{k} \left(n_j - \frac{n}{k} \right)^2 . \tag{3.2}$$

Here n is the total number of all samples, n_j is the number of samples in the sector S_j . Thus, using the formula 3.2, we can numerically express how much spherically symmetric is the distribution of events around the studied point.

As mentioned earlier, we do not know for sure which shape the projection of the calibration source on the plane (the CSE) would have (circle or ellipse). We only have an expectation that these will be ellipses based on the features of the detector. It is a well known fact that the tracking works more precisely in the y-direction than in the z-direction. Therefore, it is expected that the track fit uncertainty along the z-axis will be greater than along the y-axis. The shape of the projection should depend on these uncertainties around the plane x = X_0, and in this case we should observe ellipses with the semi-major axis along the z-direction.

In order to profit from this method in my project, it was necessary to abandon the strict idea of spherical symmetry because ellipse is not spherically symmetric. If we fix the number of sectors to only 4, then as can be seen from the figure 3.5b, both the circle and the ellipse will have the same quadrupolar symmetry around (y_0, z_0) because the areas of each of the four sectors are the same. The circular symmetry is not tested anymore, nevertheless the goal is only to find the best possible value of the center. Even in the case of an elliptic form of the source projection, it is possible to apply an approach using the estimate from equation 3.2. By variation of the center (y_0, z_0) of the sample statistics (the statistics inside of the ellipse or circle) we can always obtain a χ^2 / n.d.f. (number degrees of freedom) based on the equation for each such point. If the value of χ^2 / n.d.f. is low then the sample statistics express a high degree of quadrupolar symmetry and its central point is the most probably the real center of the CSE.

Inspired by the method in [46] I proposed an algorithm to find a center of any CSE for given plane (at coordinate x) and for a given source:

- The hotspot area shown in figure 3.2 is divided into 14 equal rectangular zones. As a result, each zone will contain one CSE which represents one source.

- For each individual rectangle, the center of mass (y_{CM}, z_{CM}) of the sample

is found. This is a rough estimation of the position of the CSE to estimate the closest CSE´s vicinity.

- The regular grid of (y_i, z_i) values in the vicinity of the point (y_{CM}, z_{CM}) is selected. These centers are studied whether they are the centers of a quadrupolar symmetry. The grid dimensions are 40 mm × 40 mm, the distance between adjacent points (y_i, z_i) is 0.2 mm in both directions.

- Using the equation 3.2 we find the χ^2 / n.d.f. value for each of the points (y_i, z_i) from the grid. The result of the evaluation can be seen in the figure 3.6.

- The centre of source is considered to be the point (y_i, z_i) with the smallest χ^2 / n.d.f.. The point is denoted as (y_C, z_C).

- The process is repeated for all the sources for each of the desired planes defined by x-coordinate.

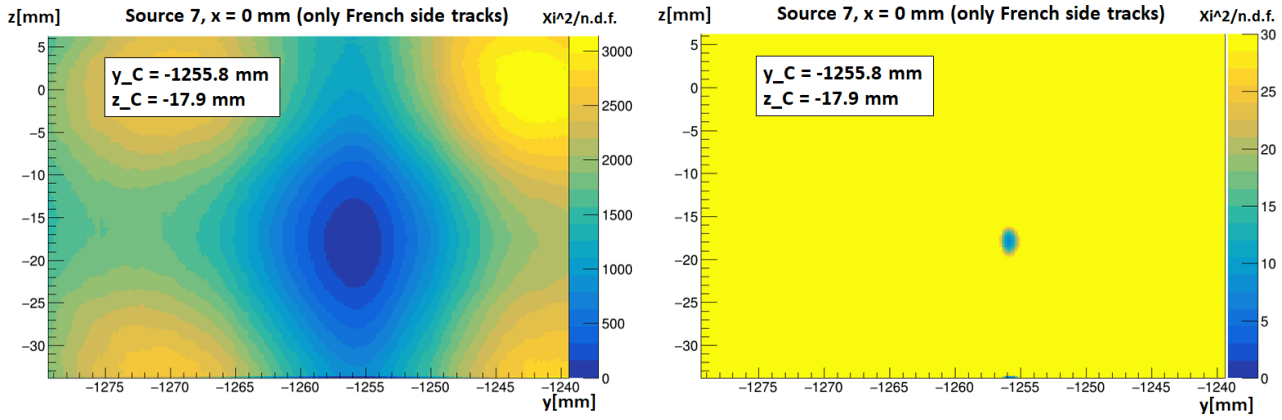

(a) (b)

Figure 3.6: Two-dimensional χ^2 / n.d.f. distributions. Each point represents a value of χ^2 / n.d.f. calculated by equation 3.2 for a given center of symmetry y_i, z_i. It can be seen that the distribution in vicinity of studied CSE shows the best quadrupolar symmetry at point y_C = -1252.3 mm, z_i = -11.1 mm. (a) Colour scale for χ^2 / ndf = 0-3100 (b) Colour scale for χ^2 / ndf = 0-30.

In practice, the algorithm can be made faster and more accurate if it is used in the form of iterations. In the first iteration we choose a bigger distance between adjacent points in the grid to quickly sample the distribution, and after the first

run of the algorithm, we will get the (y_C, z_C) with the smallest χ^2 / n.d.f.. Then we choose a new grid in vicinity of this value (y_C, z_C) with smaller dimensions and closer distance between the points. We run the algorithm again and get a new, more accurate position of the center of source. With enough iterations, we will get a precise value for the position of the center more quickly. In my approach, I learned that five iterations are sufficient.

Using all the mentioned features, for the thesis, I wrote a code implementing this algorithm. The output of the codes are the best coordinates of the center of the CSE for any plane with given x-coordinate. An example of code output (for source number 7) is shown in the figure 3.7.

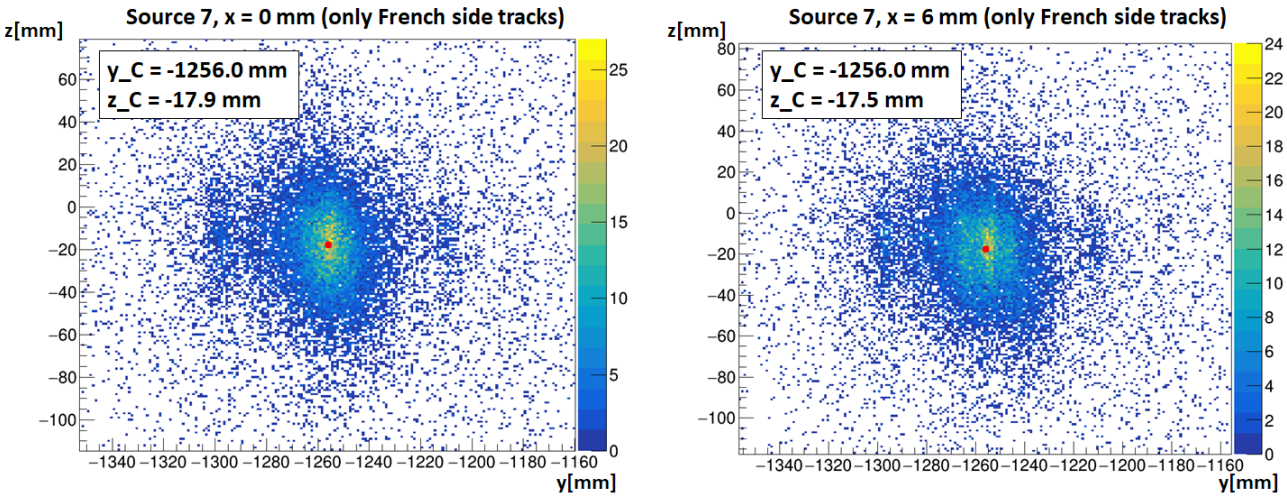

(a) (b)

Figure 3.7: The distribution of vertices in vicinity of the source number 7 for two different planes. Output of the program where the red dot indicates the position found by the algorithm (a) at x = 0 mm is (-1256.0 mm, -17.9 mm) (b) at x = 6 mm is (-1256.0 mm, -17.5 mm). You can see that the position of the center almost does not change between projections in x-planes which are close to each other.

3.5 Determination source positions in x-direction

3.5.1 Data selection

As can be seen from the figures 3.2 and 3.7 produced on the basis of the raw data, the histograms are heavily covered by "background events". This is due to several factors. The first and most important thing is that this array of data is obtained from a detector that is at the stage of commissioning. Only a third

of the detector was available and there was no shielding. The next point is that the algorithm for track reconstruction is in the stage of development and only its very first version was used. The method has still its own known limits which will be improved in future. Even in these conditions, it is already possible to obtain reasonable results and analyze them. To improve this process, we can do preliminary data selection.

In order to limit hits which most probably occurred due to misreconstruction or as a fake signal due to absence of the shielding I applied a following data cleaning process. Let us choose two planes with the corresponding x-coordinates x_L and x_R far enough from the source. We choose these values so we should be sure that the source´s X_0 coordinate (see figure 3.4a) is between them (even though we don´t know the X_0 yet precisely). We find the apparent projected position of the source in these planes and build a CSE in a form of circle using algorithm described in previous section. The radius of the circles r was chosen empirically in order to avoid most of the marginal background hits but also not to cut too much into the area of the hits from the source. Now we impose the condition on each track which would pass the elimination must pass through the first and second circle at the same time. The situation is described in the figure 3.8. The most tracks that carry information about the source will pass inside these improvised cones: "Cone 1" and "Cone 2". Tracks that fell into the area of the inclined cylinder (bounded by red dotted lines) may also remain, which will be the background but less prominent than before. The slope for the cylinder depends on the received values of the coordinates of the centers of the source projections on the selected planes.

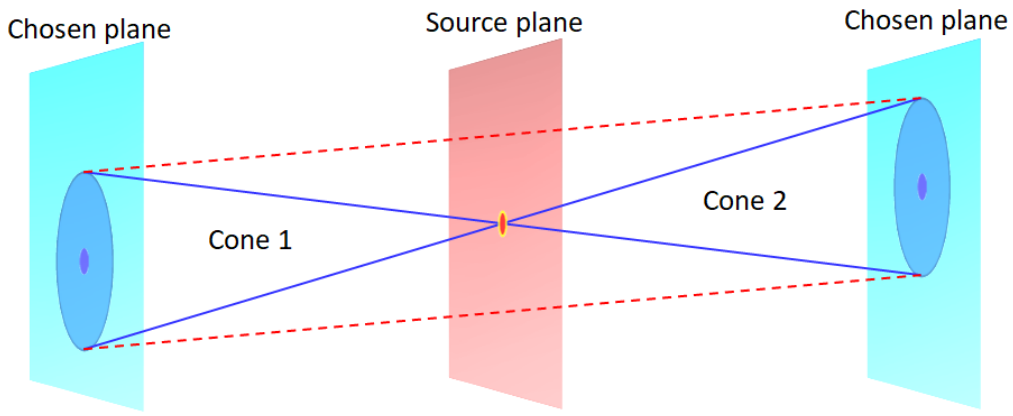

Figure 3.8: Methodology of data selection

Empirically, I chose x_L = -10mm and x_R = 10mm, and the radius of the circle r = 30 mm. The result of such "cleaning" can be seen in the figure 3.9

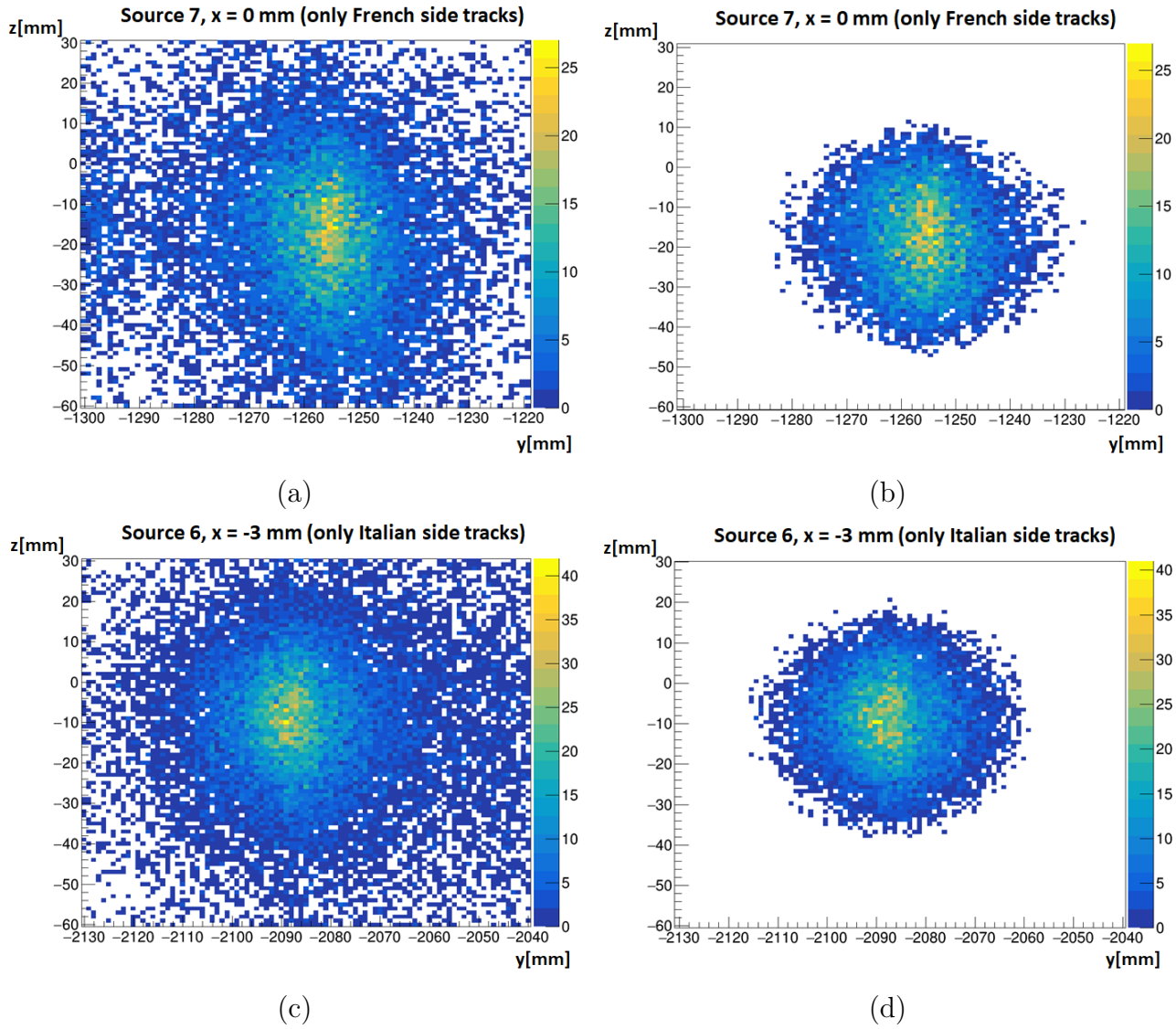

(a) (b)

(c) (d)

Figure 3.9: Views before/after data selection for (a,b) source 7 on the x = 0 mm plane (c,d) source 6 on the x = -3 mm plane

Note that, this method of data selection is empirical but quite natural at the same time. It discriminates the tracks which are too much deviating from the perpendicular direction according to the source plane. Such electrons do not follow the shortest possible distance towards main calorimeter wall and have higher chance to carry imprecisions.

3.5.2 Final results

As mentioned in the section 3.3, it is interesting to study whether X_0 coordinate of the ^{207}Bi sources is equal to 0 mm or some other value. In other words, we can formulate a null hypothesis that $X_0 = 0$ mm. We would like to test whether this null hypothesis can be rejected on a sufficient confidence level. According to the methodology explained in previous sections, it is necessary to obtain the apparent dimensions of the source projections (CSEs) in the investigated planes (figure 3.4a). As the characteristic dimensions we defined the length of semi-axes of CSEs. These values represent the accuracy of how precisely the detector "sees" the source: Δy in y-direction and Δz in z-direction. For a given CSE in a given plane defined by x-coordinate it is possible to construct projections of two-dimensional vertex distribution into axes y and z. The values of Δy and Δz, therefore, define as respective standard deviations of the two projections. My observation showed that values Δy and Δz defined as standard deviations were very dependent on the choice of the region around the CSE before application of data cleaning method introduced in the section 3.5.1. After such cleaning process, the dependence was not visible anymore. By calculation of Δy and Δz values for CSEs for all x-coordinates of the intersection planes between x_L = - 10 mm and x_R = 10 mm, with a step of ε = 0.5 mm, one obtains a pair of values Δy, Δz for each plane, i.e. for each value of coordinate x. The values Δy, Δz can be represented as two functions of coordinate x: Δy(x), Δz(x). Such dependencies can be calculated for each source separately. These dependencies can be seen in the figure 3.10

It is obvious by naked eye that the CSEs reach the minimal size near the coordinate x = 0. Let us estimate the position X_0. If we assume that all sources are in the same plane, and, therefore, have the same X_0 position, then the graphs 3.10 can be understood as an attempt to measure this coordinate in a set of repeated "experiments" (one "experiment" per source). In this case, the value of the desired "collective" X_0 can be taken as the arithmetic mean of all the minima of the curves presented in the histograms 3.10. As an estimate of precision of such approach, I also calculated the standard deviation of the distribution of the minima using the standard formula with assumption of the Bessel's correction (due to low number of experiments):

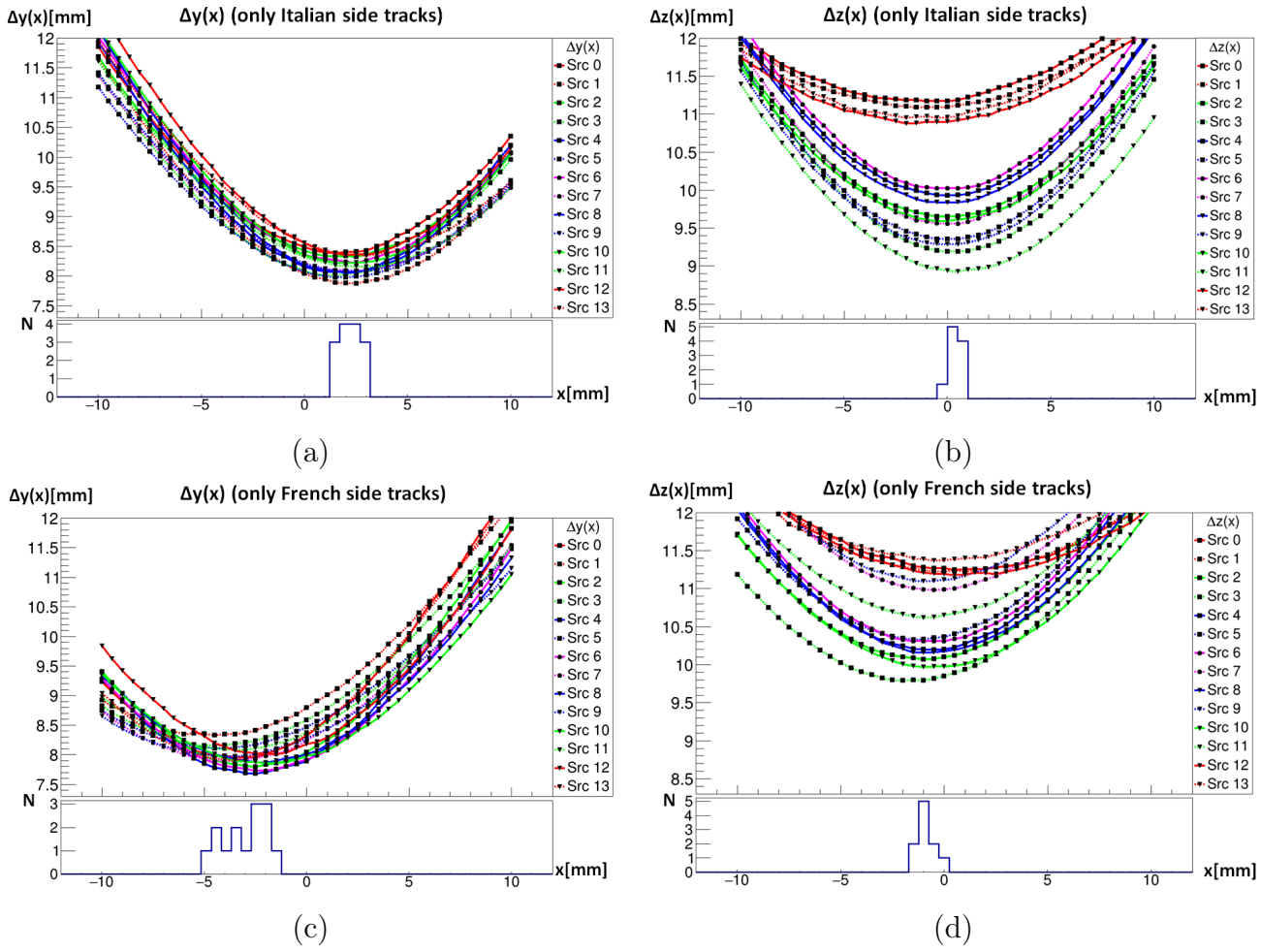

(a) (b) (c) (d)

Figure 3.10: Dependence of CSE semi-axes of the x-coordinate of the section plane. The 14 graphs in different colors represent the values for the 14 calibration sources. At the bottom of each graph is a histogram of the minimum values of the graphs of all sources. (a) Δy(x) Italian side (b) Δz(x) Italian side (c) Δy(x) French side (d) Δz(x) French side

$$s^2 = \frac{1}{n-1}\sum_{i=1}^{n}(x_i - \bar{x})^2 \tag{3.3}$$

It should be noted that the graph of the dependence of Δz(x) clearly distinguishes four sources, represented by four lines on top. They are formed by the two lowest sources (12, 13) and the highest (0, 1) - see figure 3.2. Their higher uncertainty in the z-direction, compared to the other sources, is expected. It can be explained by the fact that the reconstruction of the track of a particle which passes close to the ends of anodes of the Geiger cell is less accurate (the electric field is there less symmetric). I did not take the results in z-direction into account in case of these sources.

The obtained values for the mean value of the collective X_0 and its confidence interval are listed in the following table 3.1:

	Δy(x)	Δz(x)
Italian side	$\bar{X_0}$ = 2.25 $\pm$ 0.55 mm	$\bar{X_0}$ = 0.15 $\pm$ 0.34 mm
French side	$\bar{X_0}$ = -3.07 $\pm$ 1.11 mm	$\bar{X_0}$ = -0.9 $\pm$ 0.46 mm

Table 3.1: Values for the mean x-coordinate value and standard deviation for the corresponding projection and detector side

If we look at the values in the last column (obtained by using the plots for Δz(x)) we see that the data obtained by Italian side detector (first row) as well as the one from French side (second row) of the detector are consistent with X_0 = 0 mm within 2σ. The case of the data from Δy(x) seems to express more of the deviation from X_0 = 0 mm. The deviations are on the level of 2.76σ and 4.09σ for French and Italian side data, respectively. This deviation is relatively significant, nevertheless, it is not clear why it differs so much to the case of Δz(x)). This might be due to some systematic biases which were unintentionally introduced in the analysis process or due to the quality of the data. It is clear that more insight is needed. I suggest to repeat the study with data set where the full tracker was operational and all 42 sources were deployed. It would be also ideal to collect statistics for longer than 2.5 hours. Finally, new version of the track fitting algorithm could be used. Such improvements should, hopefully, shed more light on this situation. For the purpose of this work, I consider the "null hypothesis" as accepted. For the purpose of calculation of recommended Y_0 and Z_0 coordinates for each of the sources I took X_0 = 0 mm as the position of the source in the x direction.

3.6 Determination of the position of the source in yz-plane

After acceptance of the null hypothesis X_0 = 0 mm it is now clear which plane is the best to use to properly extract the coordinates Y_0 and Z_0 of the ^{207}Bi sources. By study of CSEs in the plane x = 0 the Y_0, Z_0 source coordinates were obtained by method presented in the section 3.4. The uncertainties Δy, Δz of these coordinates were extracted using the methodology in the section 3.5. This

section also describes the data pre-cleaning algorithm which was applied before the calculation. The final results are presented in the table 3.2.

1^{st} column			2^{nd} column		
No.	**Y_0 [mm]**	**Z_0 [mm]**	**No.**	**Y_0 [mm]**	**Z_0 [mm]**
0	-2088.8 ± 8.3	1404.7 ± 10.3	**1**	-1254.6 ± 8.3	1405.2 ± 10.4
2	-2088.6 ± 8.3	942.0 ± 9.9	**3**	-1254.5 ± 8.4	940.8 ± 9.5
4	-2088.2 ± 8.1	470.0 ± 10.1	**5**	-1253.6 ± 8.4	465.5 ± 9.9
6	-2088.3 ± 8.2	-9.1 ± 10.2	**7**	-1253.9 ± 8.4	-13.7 ± 10.3
8	-2088.5 ± 8.2	-484.4 ± 10.0	**9**	-1253.4 ± 8.3	-487.4 ± 10.1
10	-2088.2 ± 8.2	-952.4 ± 9.8	**11**	-1252.9 ± 8.4	-955.2 ± 9.8
12	-2087.3 ± 8.2	-1407.6 ± 10.1	**13**	-1251.9 ± 8.3	-1407.0 ± 10.4

Table 3.2: Recommended Y_0 and Z_0 coordinates for each of the sources for taken $X_0 = 0$ mm as the position of the source in the x direction. The first and fourth columns indicate the number of the calibration source defined in 3.2

The table shows that the horizontal distances between pairs of two sources in one row are ranging from 834.0 mm (sources 2 and 3) to 835.4 mm (sources 12 and 13) which is a distance very similar to the design value of 835 mm. If we consider couples of sources neighbouring in one column, their vertical differences range from 451.8 mm (sources 11 and 13) to 479.2 mm (sources 5 and 7). These values are also consistent with the design values of 475 mm. In fact, if we remove the sources 0, 1, 12 and 13 on top and bottom from the consideration due to higher uncertainty of their z-coordinates, we obtain the differences very close to the value of 475 mm. It seems that the method is already relatively powerful despite the fact that there are many more details to improve. The values from table 3.2 should be consider as recommended values for the source positions (along with $X_0 = 0$ mm) for any practical purposes.

3.7 Conclusions and outlook

The thesis was dedicated to a very first study of the positions of the ^{207}Bi calibration sources in SuperNEMO detector. It was shown that the methodology proposed in the thesis has a potential to measure detector dimensions with precision of millimeters or better. The main goal of the thesis was to experimentally measure

the positions of 14 ^{207}Bi calibration sources. These values summarized in table 3.2, along with $X_0 = 0$ will serve as recommended values of the source coordinates. These values will be used by the collaborators for application of improved data cuts for the energy calibration script. They will be crucial for the improvement of energy corrections in the calibration process. I also conclude that no statistically significant deviation from SuperNEMO design blueprints were observed for the measured quantities.

The study also shown several possibilities for improvement of the method. In the future, it will be very important to repeat the study with all 42 sources. I also suggest to use a data run which is longer than 2.5 hours used in this thesis. In months to follow, it is expected that new, more precise version of electron tracking algorithm (based on the Legendre transform) will be released by collaborators. Finally, in 2024 the detector should be operated with the full shielding. This should help to suppress background counts and also improve the study in the near future.

References

(1) L'Annunziata, M. F., *Handbook of Radioactivity Analysis (Third Edition)*, Third Edition; L'Annunziata, M. F., Ed.; Academic Press: Amsterdam, 2012, pp 3–10.

(2) Chadwick, J. *Verhandlungen der Deutschen Physikalischen Gesellschaft* **1914**, 383–391.

(3) Pauli, W. *Phys. Today* **1978**, *31N9*, 27.

(4) Chadwick, J. *Nature* **1932**, *129*, 312.

(5) Cowan, C. L.; Reines, F.; Harrison, F. B.; Kruse, H. W.; McGuire, A. D. *Science* **1956**, *124*, 103–104.

(6) Iliadis, C., *Nuclear Physics of Stars*, 2007; Chapter 5.

(7) Bahcall, J. N.; Davis, R. *Science* **1976**, *191*, 264–267.

(8) Cleveland, B. T.; Daily, T.; Raymond Davis, J.; Distel, J. R.; Lande, K.; Lee, C. K.; Wildenhain, P. S.; Ullman, J. *The Astrophysical Journal* **1998**, *496*, 505.

(9) Fukuda, Y. et al. *Phys. Rev. Lett.* **1998**, *81*, 1562–1567.

(10) Ahmad, Q. R. et al. *Phys. Rev. Lett.* **2001**, *87*, 071301.

(11) Lipari, P. In *1st CERN-CLAF School of High-Energy Physics*, 2001, pp 115–199.

(12) Goeppert-Mayer, M. *Phys. Rev.* **1935**, *48*, 512–516.

(13) Furry, W. H. *Phys. Rev.* **1939**, *56*, 1184–1193.

(14) Shtembari, L. *PoS* **2022**, *ICHEP2022*, 614.

(15) Barabash, A. S.; Brudanin, V. B. *Phys. Atom. Nucl.* **2011**, *74*, 312–317.

(16) Azzolini, O. et al. *Phys. Rev. Lett.* **2019**, *123*, 262501.

(17) Arnold, R. et al. *Eur. Phys. J. C* **2019**, *79*, 440.

(18) Waters, D. *J. Phys. Conf. Ser.* **2017**, *888*, 012033.

(19) Le Noblet, T. *J. Phys. Conf. Ser.* **2020**, *1342*, ed. by Clark, K.; Jillings, C.; Kraus, C.; Saffin, J.; Scorza, S., 012029.

(20) *PoS* **2022**, *ICHEP2022*, 552.

(21) Gando, A. et al. *Phys. Rev. Lett.* **2016**, *117*, 082503.

(22) Yuto, K. *J. Phys. Conf. Ser.* **2021**, *2156*, 012230.

(23) Biancacci, V. *PoS* **2022**, *EPS-HEP2021*, 800.

(24) Ackermann, K. H. et al. *Eur. Phys. J. C* **2013**, *73*, 2330.

(25) Guiseppe, V. et al. In *2008 IEEE Nuclear Science Symposium Conference Record*, 2008, pp 1793–1798.

(26) Bhang, H. et al. *Journal of Physics: Conference Series* **2012**, *375*, 042023.

(27) Zolotarova, A. *Proc. 53rd Int. Conf "Rencontres de Moriond – EW 2018" (2018 Electroweak Interactions and Unified Theories), ARISF* **2018**, 445–448.

(28) Arnaboldi, C. et al. *Nuclear Instruments and Methods in Physics Research Section A: Accelerators, Spectrometers, Detectors and Associated Equipment* **2004**, *518*, 775–798.

(29) Gando, Y. et al. *JINST* **2021**, *16*, P08023.

(30) Ajimura, S. et al. *Phys. Rev. D* **2021**, *103*, 092008.

(31) Auger, M. et al. *JINST* **2012**, *7*, P05010.

(32) Ackerman, N. et al. *JINST* **2022**, *17*, P02015.

(33) Arnold, R. et al. *Nuclear Instruments and Methods in Physics Research Section A: Accelerators, Spectrometers, Detectors and Associated Equipment* **2005**, *536*, 79–122.

(34) Arnold, R. et al. *Eur. Phys. J. C* **2010**, *70*, 927–943.

(35) Gomez-Cadenas, J. J. *Nucl. Part. Phys. Proc.* **2016**, *273-275*, ed. by Aguilar-Benıtez, M.; Fuster, J.; Martı-Garcıa, S.; Santamarıa, A., 1732–1739.

(36) Rodejohann, W. *International Journal of Modern Physics E* **2012**, *20*.

(37) Rakhimov, A. V. et al. *Radiochimica Acta* **2020**, *108*, 87–97.

(38) Cascella, M. *Nucl. Instrum. Meth. A* **2016**, *824*, ed. by Bisogni, M. G.; Grassi, M.; Incagli, M.; Paoletti, R.; Signorelli, G., 507–509.

(39) Barabash, A. et al. *Nuclear Instruments and Methods in Physics Research Section A: Accelerators, Spectrometers, Detectors and Associated Equipment* **2017**, *868*, 98–108.

(40) Hodák, R. et al. *AIP Conf. Proc.* **2015**, *1672*, ed. by Orrell, J. L., 130003.

(41) Salazar, R.; Bryant, J. *PoS* **2017**, *ICHEP2016*, 808.

(42) Collaboration, S. et al. *Journal of Instrumentation* **2021**, *16*, T07012.

(43) Cascella, M.; Chopra, A.; Dawson, L. *J. Phys. Conf. Ser.* **2017**, *888*, 012249.

(44) Brun, R.; Rademakers, F. *Nuclear Instruments and Methods in Physics Research Section A: Accelerators, Spectrometers, Detectors and Associated Equipment* **1997**, *389*, New Computing Techniques in Physics Research V, 81–86.

(45) Alexopoulos, T.; Bristogiannis, Y.; Leontsinis, S. Track reconstruction through the application of the Legendre Transform on ellipses, 2016.

(46) Rattihalli, R. N.; Rao, K. S. M.; Raghunath, M. *Communications in Statistics - Simulation and Computation* **2019**, *48*, 922–943.